Slow L-H Transitions in DIII-D Plasmas

R. J. Colchin,[1] M. J. Schaffer,[2] B. A. Carreras,[1] G. R. McKee,[3] R. Maingi,[1] T. N. Carlstrom,[2] D. L. Rudakov,[4] C. M. Greenfield,[2] T. L. Rhodes,[5] E. J. Doyle,[5] N. H. Brooks,[2] and M. E. Austin[6]

[1]*Oak Ridge National Laboratory, Oak Ridge, Tennessee 37831-8072*
[2]*General Atomics, P.O. Box 85608, San Diego, California 92186-5608*
[3]*University of Wisconsin, Madison, Wisconsin 53706*
[4]*University of California at San Diego, La Jolla, California 92093-0319*
[5]*University of California at Los Angeles, Los Angeles, California 90095*
[6]*University of Texas, Austin, Texas 78712*

(Received 24 September 2001; published 6 June 2002)

The transition from the low to the high mode of plasma confinement (L-H transition) is studied in the DIII-D by an experimental technique which allows an arbitrarily slow transition. During an initial transition, periodic turbulent instability bursts are observed near the separatrix which inhibit the full transition. These bursts are damped by self-generated shear flows, and a predator-prey-type relationship is shown to give a good description of the data. As the neutral-beam power is raised, the oscillations change to type III edge localized modes. Another transition then leads to a quiet H mode.

DOI: 10.1103/PhysRevLett.88.255002 PACS numbers: 52.55.Fa

Magnetic fusion reactors are designed to operate in the high-confinement mode (H mode) [1] regime. Although studied extensively, both theoretically [2] and experimentally [3], the physics of the transition to the H mode is not well enough understood to confidently predict the amount of auxiliary power necessary to ensure the transition [4] in fusion reactors. The transition usually takes place quickly, which has inhibited study of the transition mechanism. In DIII-D experiments, we have been able to control the transition by carefully adjusting the input power. We find that the transition can be characterized by two phases. The first of these phases is characterized by an oscillatory behavior of the edge plasma. The second phase corresponds to a fast transition to type III edge localized modes (ELMs), followed by a quiet H mode. This second transition has not been controlled by adjustment of the input power. The behavior of these two transition phases is consistent with the first being a second-order transition and the second being a first-order transition [5]. A second-order transition is such that the order parameter (the shear flow) is a continuous function of the control parameter (power absorbed), while the first-order transition is discontinuous. For the second-order transition, the transition time goes to infinity when the control parameter is at its critical value. This is not the case for a first-order transition. Because of the difficulty of measuring the shear flow in a continuous manner, we use the latter property as a way of identifying the type of transition.

The initial phase of the transition has been dubbed the IM mode, since it is an intermediate confinement regime between that of the L and the H modes. The IM mode has been obtained in lower single-null DIII-D plasmas having a plasma current of 1 MA and a toroidal field of 2.14 T. Sustained IM modes were obtained when the X-point was $\sim$9.3 cm from the divertor floor and the neutral beam power was maintained above the IM-mode threshold of $P \approx 300$ kW. This phase can be prolonged indefinitely by maintaining the input power in a range of $\Delta P \approx 300-500$ kW above the threshold. When the X-point was raised to 17.6 cm, the IM mode was obtained only briefly.

Transitional modes similar to the IM mode have been observed previously [6–8] and have been associated with "dithering." Detailed experimental evidence shows no tendency for the plasma confinement in the IM mode to oscillate between the H and the L regimes (L = low). The IM mode is observed during both the L-H and the H-L transitions.

The IM mode is characterized by periodic bursts of an instability near the outer plasma edge. These bursts initiate oscillations of the D_α light which are present and in phase on all D_α detectors, but are of largest amplitude on a detector which views the outer divertor along a flux surface originating near the outer-midplane separatrix and ending outside the outer divertor strike point. The first three traces of Fig. 1 show the D_α signal, the neutral beam power, and the line-averaged density. The D_α signal begins in the L mode. The neutral beam power is stepped up to 500 kW and after a short time the transition to the IM mode occurs, accompanied by fluctuations in the D_α signal. Later in time as the fluctuations increase in amplitude and break up, type III ELMs appear, followed by a quiet H mode. The density initially rises and then remains constant until the IM-mode oscillations begin to break up.

The bottom two traces of Fig. 1 show the D_α oscillations on an expanded time scale. The first trace is taken from near the start of the IM mode and shows regular oscillations of 1.6 kHz. As the injection power is increased, the oscillation frequency decreases to $\sim$1.1 kHz. As shown in the bottom trace, the leading edge of the oscillations becomes steeper, and the oscillatory coherence is lost as

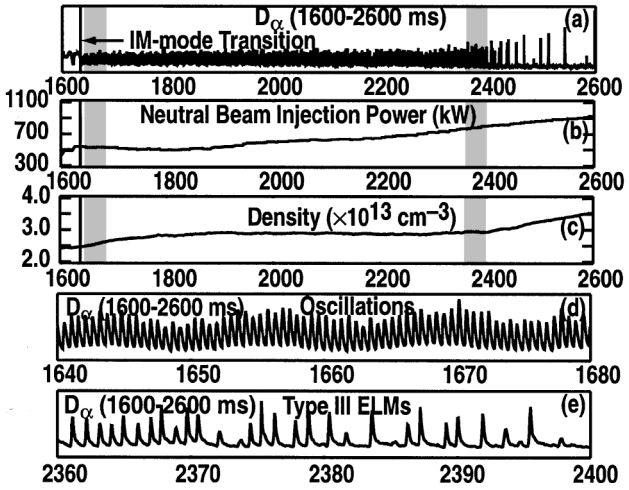

FIG. 1. (a) D_α from a light cone looking along a divertor flux surface which originates close to the outer separatrix. The L mode is at the left, followed by (at the vertical line) the oscillatory IM mode, and finally the quiet H mode on the right. (b) The neutral beam power. (c) The line-averaged density. (d) D_α oscillations on an expanded scale, at the beginning of the IM mode [initial shaded area in traces (a)–(c)]. (e) D_α oscillations on an expanded scale, toward the end of the IM mode become type III ELMs [later shaded area in traces (a)–(c)].

the transition is made to type III ELMs. This sequence of events is repeated in reverse at the H-L transition.

Signals from the instability are observed on a number of radially resolved diagnostics located near the midplane of DIII-D. These include beam emission spectroscopy (BES) [9], microwave reflectometers, electron cyclotron emission, a radial array of eight D_α detectors, and a plunging probe [10]. All diagnostics agree that the instability is located in the radial region between normalized minor radii of $\rho = 0.98$–1.0 [$\rho \equiv 1 + (R - R_{\text{out}})/a$], and that the instability burst duration is approximately 300 μs, which is a fraction of the D_α oscillation period. Data from a plunging probe penetrating just inside the separatrix, showing the rms value of the instability driven temperature fluctuations $\tilde{T}_e$, is plotted in Fig. 2. Also plotted as a time reference is the D_α signal.

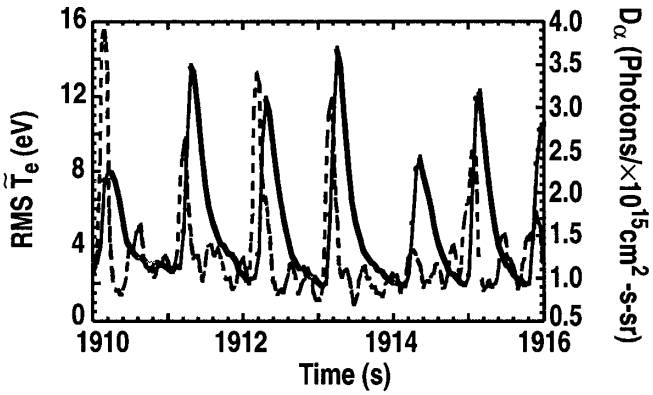

FIG. 2. Root-mean-square instability electron temperature fluctuations (dashed line) from a plunging probe located just inside the separatrix. D_α fluctuations (solid line) are plotted as a time marker.

Magnetic pickup coils located at the midplane record magnetic fluctuations of less than a gauss and indicate the weak magnetic character of the instabilities. Currents flowing to the divertor target tiles are synchronized with the instability bursts, and are observed on tiles located all around the machine, suggesting that the instability is toroidal in nature. Langmuir probes located in the divertor target see details of the instability fluctuations, indicating good electrical connection along flux surfaces between the midplane scrapeoff layer (SOL) and the floor.

Electron temperature and density data fits from Thomson scattering are shown in Fig. 3. Four lasers are fired in succession, and are timed to encompass a single D_α oscillation, as shown in the upper right-hand corner insets. The instability burst takes place during the second (blue-marker) laser firing. The N_e and T_e profiles of Fig. 3 are not appreciably affected by the instabilities, except that the density and temperature are raised somewhat around the separatrix and in the SOL region. There is no evidence that the instability is stabilized by profile erosion. Dur-

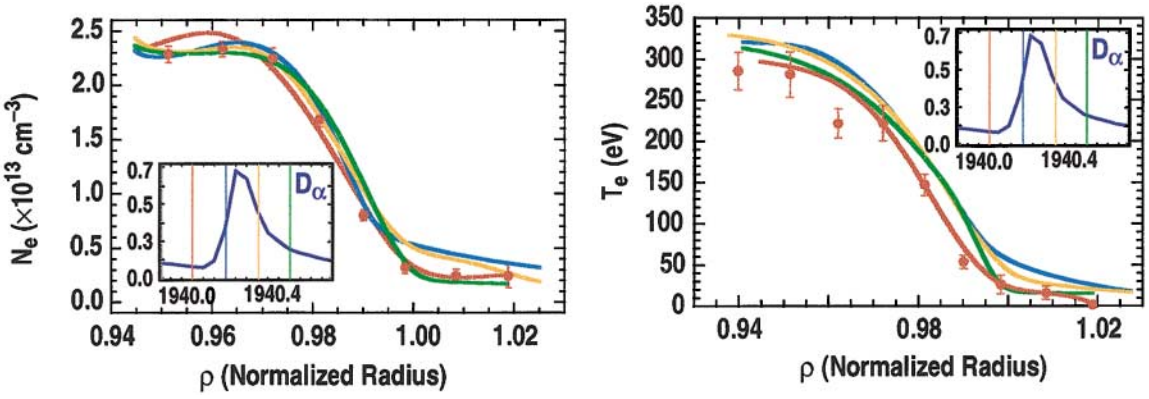

FIG. 3 (color). Fits to Thomson scattering N_e and T_e data taken at 4 times during a D_α oscillation. Times relative to the oscillation are shown in the insets and are color coded. The normalized radius $\rho \equiv 1 + (R - R_{\text{out}})/a$, where a is the minor radius and R_{out} is the outer major radius. Error bars shown on data from the initial laser pulse represent typical photon statistics.

ing the whole *IM* phase, density profiles remain invariant while T_e and T_e gradients are observed to increase steadily. As a result, the plasma pressure and pressure gradients increase during the *IM* mode.

Data from the midplane BES diagnostic reveal details of the mode's density fluctuations. Figure 4(a) shows data from one BES channel located at the separatrix during one instability burst. Also plotted is the rms $\tilde{T}_e$ signal (Fig. 2). Shown for timing comparison is data from the D_α signal. The mode is observed to grow and to damp in times of $\sim$150 μs. Data points used to measure the growth and damping rates are shown by triangles and solid circles, respectively. During the burst, some density is ejected radially into the SOL as shown in Fig. 4(b) and also by the Thomson scattering [(Fig. 3(a)]. Bursts of electron temperature and density are additionally observed by a midplane plunging probe, coincident with the D_α signal rise. Poloidally spaced BES detectors show that the mode is rotating in the electron diamagnetic direction. By observing the time delay between two BES channels spaced poloidally by 1 cm, it is possible to interpret the data as a rotation velocity as shown in Fig. 4(c). This measurement is affected by plasma noise, which restricts the measurement time to the high-growth portion of the instability (after 0.16 ms). During the mode-damping portion of the burst (after 0.21 ms), the rotation velocity is observed to increase by as much as a factor of 3.

The features of these repetitive bursts are found to be described by equations of the predator-prey type, formulated in Ref. [11], for the coupling between fluctuations and shear flow. This coupling is the basis for one of the *L-H* transition models [12]. These models assume that the growth of the instability is driven by its average gradient and is subsequently damped due to self-generated shear flows. This process leads to periodic instability growth and damping and can be independent of the specific nature of the instability. We use the formalism of Ref. [11], where the "predator" is the self-generated shear flow rate Ω_s normalized by the frequency $\overline{\omega} \approx \sqrt{\gamma\mu}$. Here μ is the shear-flow damping rate and γ is the instability growth rate. The frequency of the oscillations is $\overline{\omega}$. Equations which describe the oscillations are

$$\frac{d\Omega_s^2}{dt} = 2(\overline{a}\tilde{T}^2 - \mu)\Omega_s^2, \tag{1}$$

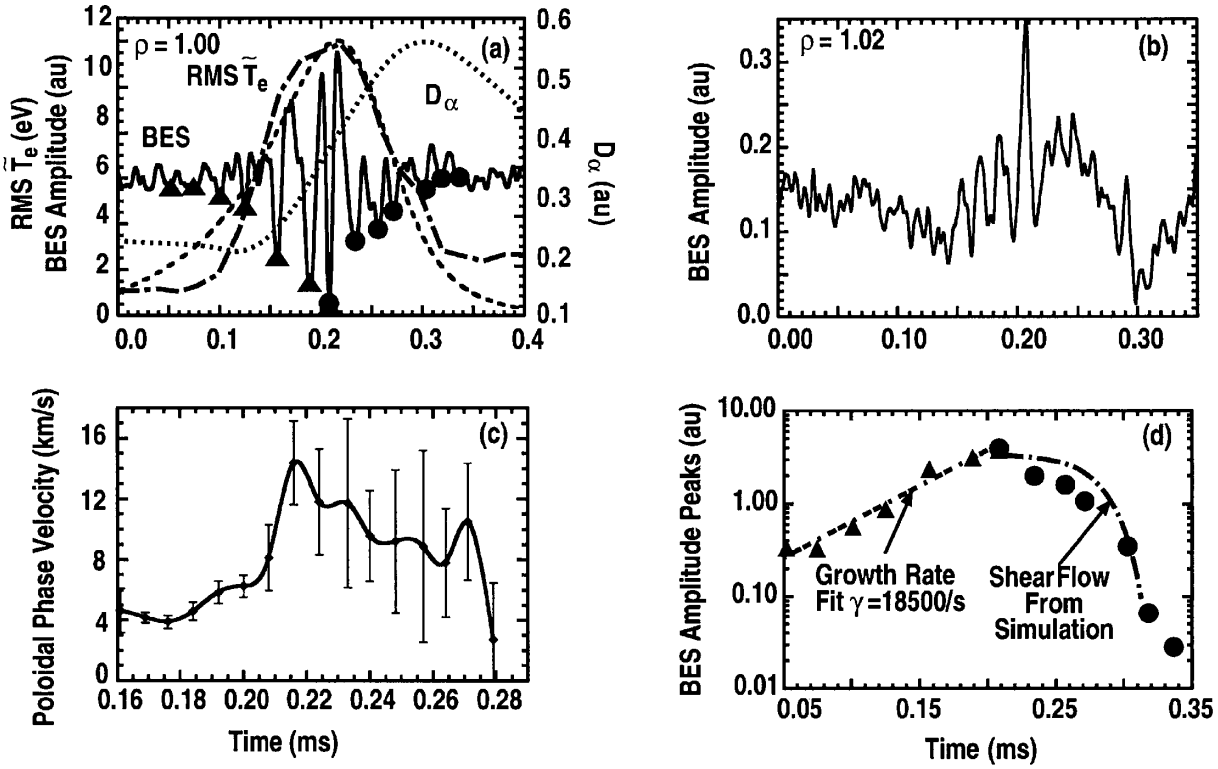

FIG. 4. (a) BES (solid line), rms $\tilde{T}_e$ temperature fluctuation (dashed line), predator-prey model rms $\tilde{T}_e$ (long/short-dashed), and D_α (dots) data during an instability burst. Data points used to measure the growth (triangles) and damping (circles) rates are shown. BES channel 18, located at a normalized radius of $\rho = 1.00$. BES and probe data are from consecutive shots, time aligned by the D_α bursts. (b) BES channel 23 data, located at $\rho = 1.02$, radially adjacent to BES channel 18. (c) Poloidal velocity averaged over four BES channels centered around channel 18. Note the time scale change from the other figures. Error bars are standard deviations of the data and are larger at higher velocities due to a 1 μs digitization rate limit. (d) Exponential fit to the growth rate data points (triangles) from (a), and the damping calculated from the predator-prey model compared to the data points (circles) shown in trace (a). The linear correlation coefficient for the growth rate fit was 0.976.

$$\frac{d\tilde{T}^2}{dt} = 2\left(\gamma - \frac{\overline{\omega}}{4}\,\Omega_s^2\right)\tilde{T}^2, \qquad (2)$$

where $\overline{a}$ is related to the shear-flow growth rate.

Figure 4(d) shows a fit to the growth rate derived from the data of Fig. 4(a), yielding $\gamma = 18\,500\ \mathrm{s}^{-1}$. Initial conditions $\dot{\Omega}_s(t=0) = \dot{\tilde{T}}_e(t=0) = 0$ yield $\overline{a}(t=0) = \mu/\tilde{T}_{e0}^2$ and $\Omega_s(t=0) = \sqrt{4\gamma/\overline{\omega}}$.

Using the initial conditions, Eqs. (1) and (2) may be solved numerically. A fit to the measured rms $\tilde{T}_e$ is obtained [see Fig. 4(a)] for an initial value of $\tilde{T}_{e0} \approx 10$ eV. The frequency of the oscillations at the time of the data in Fig. 4 was $f = 1200$ Hz. The best match to this oscillation frequency was obtained for $\mu = 1700\ \mathrm{s}^{-1}$.

Figure 4(d) shows the mode-damping data points from Fig. 4(a). Calculated shear-flow values during a half of a cycle of the shear flow are added for comparison showing qualitative agreement with the experimental data. This agreement, coupled with data of Fig. 4(c) which suggest a tripling of the flow rate of the plasma at the separatrix during the mode damping, are indications that self-generated shear flow is the mechanism responsible for damping the observed modes. Several features observed experimentally are mimicked by the predator-prey calculations, including small amplitude regular oscillations near onset, and the rise time of the oscillations becoming steeper and their frequency slowing as $\tilde{T}_e$ increases.

In summary, a new regime intermediate in character between the L and H modes (IM mode) has been discovered on DIII-D. The presence of this regime has enabled us to explore some details of the instability mode responsible for inhibiting the L-H transition during the IM mode.

During the IM-mode regime, the pressure profiles near the separatrix become steeper as the neutral beam power increases. The final transition to the H mode occurs when the pressure gradient is close to that of the H mode. These results fit into a picture of the L-H transition having two distinct phases [12,13]. In this model, the first phase is the result of a second-order transition [5], consistent with the careful adjustment of the input power necessary to control the duration of the phase. This transition is initiated when the turbulence-induced shear flow amplification (through Reynolds stress) exceeds the poloidal flow damping. Poloidal sheared flow is generated and dominates the radial electric field gradient. In this IM-mode phase, the predator-prey model describes the process: That is, there are instability bursts, and the shear flow and fluctuations increase with the neutral beam power. This results in the pressure gradient increasing, causing the radial electric field to increase. As the radial electric field gradient increases, the turbulent fluctuations are partially suppressed causing a transition to type III ELMs. Further suppression causes a first-order transition [5] to the H mode. The important point of these experiments is that they allow a detailed view of the intermediate phase.

The observed IM-mode relaxation oscillations are consistent with a predator-prey formalism. The model predicts the burstlike nature of the instabilities and the reduction in the frequency of the bursts as the neutral beam power is increased (as a result of an increase in $\tilde{T}_e$). The "prey" (instability $\tilde{T}_e$ fluctuations) is observed directly by a plunging probe. The predator (shear flow) is not observed directly but is inferred from BES data which show an increase in the mode's poloidal phase velocity when the mode damps, plunging probe data which show the presence of $\sim$200 V bursts of potential and potential gradients, and qualitative agreement between the observed BES damping rate and the model shear flow rate. It may be noted that self-generated shear flows have been observed under similar conditions on the H-1 heliac [14].

We thank the DIII-D team for operating the experiment. This work was supported by the U.S. Department of Energy under Contracts No. DE-AC03-99ER54463 and No. DE-AC05-00OR22725, and Grants No. DE-FG03-96ER54373, No. DE-FG03-95ER54294, No. DE-FG03-01ER54615, and No. DE-FG03-97ER54415.

[1] F. Wagner *et al.,* Phys. Rev. Lett. **49**, 1408 (1982).
[2] K. Itoh, Plasma Phys. Controlled Fusion **36**, A307 (1994), and references therein.
[3] K. H. Burrell, Plasma Phys. Controlled Fusion **36**, A291 (1994), and references therein.
[4] T. Fukuda *et al.,* Nucl. Fusion **37**, 1199 (1997).
[5] E. M. Lifshitz and L. P. Pitaevskii, *Statistical Physics, Part 1* (Pergamon Press, New York, 1980), p. 446.
[6] H. Zohm *et al.,* Plasma Phys. Controlled Fusion **37**, 437 (1995).
[7] H. Zohm *et al.,* IPP 1/276 Max-Planck-Institut Für Plasmaphysik, 1993.
[8] H. Zohm *et al.,* Phys. Rev. Lett. **72**, 222 (1994).
[9] G. McKee *et al.,* Rev. Sci. Instrum. **70**, 913 (1999).
[10] R. J. Colchin *et al.,* Nucl. Fusion (to be published).
[11] J.-N. Leboeuf, L. A. Charlton, and B. A. Carreras, Phys. Fluids B **5**, 2959 (1993).
[12] P. H. Diamond *et al.,* Phys. Rev. Lett. **72**, 2565 (1994).
[13] B. A. Carreras *et al.,* Phys. Plasmas **1**, 4014 (1994).
[14] D. L. Rudakov, M. G. Shats, and J. H. Harris, Plasma Phys. Controlled Fusion **43**, 559 (2001).